Big Galaxies and Big Black Holes: The Massive Ends of the Local Stellar and Black Hole Mass Functions and the Implications for Nanohertz Gravitational Waves

Emily R. Liepold[1] and Chung-Pei Ma[1,2]
[1] Department of Astronomy, University of California, Berkeley, CA 94720, USA; emilyliepold@berkeley.edu
[2] Department of Physics, University of California, Berkeley, CA 94720, USA

Abstract

We construct the $z = 0$ galaxy stellar mass function (GSMF) by combining the GSMF at stellar masses $M_* \lesssim 10^{11.3} \, M_\odot$ from the census study of Leja et al. and the GSMF of massive galaxies at $M_* \gtrsim 10^{11.5} \, M_\odot$ from the volume-limited MASSIVE galaxy survey. To obtain a robust estimate of M_* for local massive galaxies, we use MASSIVE galaxies with M_* measured from detailed dynamical modeling or stellar population synthesis modeling (incorporating a bottom-heavy initial mass function) with high-quality spatially resolved spectroscopy. These two independent sets of M_* agree to within ∼7%. Our new $z = 0$ GSMF has a higher amplitude at $M_* \gtrsim 10^{11.5} \, M_\odot$ than previous studies, alleviating prior concerns of a lack of mass growth in massive galaxies between $z \sim 1$ and 0. We derive a local black hole mass function (BHMF) from this GSMF and the scaling relation of supermassive black holes (SMBHs) and galaxy masses. The inferred abundance of local SMBHs above ∼$10^{10} \, M_\odot$ is consistent with the number of currently known systems. The predicted amplitude of the nanohertz stochastic gravitational-wave background is also consistent with the levels reported by Pulsar Timing Array teams. Our $z = 0$ GSMF therefore leads to concordant results in the high-mass regime of the local galaxy and SMBH populations and the gravitational-wave amplitude from merging SMBHs. An exception is that our BHMF yields a $z = 0$ SMBH mass density that is notably higher than the value estimated from quasars at higher redshifts.

Unified Astronomy Thesaurus concepts: Stellar mass functions (1612); Stellar masses (1614); Gravitational wave sources (677); Supermassive black holes (1663)

1. Introduction

The galaxy stellar mass function (GSMF) specifies the number density of galaxies as a function of their stellar masses at a given redshift. It provides an important characterization of the demographics of galaxies. As galaxies acquire stellar mass via accretion, mergers, and star formation, the shape and amplitude of the GSMF change with time. Accurately measured GSMFs at different redshifts therefore inform how galaxies grow and represent a key observational property that must be reproduced in a successful theoretical model or numerical simulation of galaxy formation and evolution. The GSMF can also be used to infer the black hole mass function (BHMF) because of the strong correlation between the masses of local galaxies and their central supermassive black holes (SMBHs).

Leja et al. (2020) present a recent census of the GSMF spanning the redshift range of $0.2 < z < 3$. Their GSMF is built from ∼10^5 galaxies in the 3D-HST (Skelton et al. 2014) and COSMOS-2015 (Laigle et al. 2016) catalogs. The stellar masses are determined from the photometric properties of the galaxies through the technique of spectral energy distribution (SED) fitting. As described there, their work is built upon a rich literature of prior measurements of the GSMF from galaxies in different surveys. A major outcome of Leja et al. (2020) is a systematically higher number density of galaxies at most stellar masses and redshifts than literature measurements in the preceding decade (e.g., Li & White 2009; Pozzetti et al. 2010; Baldry et al. 2012; Santini et al. 2012; Bernardi et al.

2013; Moustakas et al. 2013; Muzzin et al. 2013; Tomczak et al. 2014; Mortlock et al. 2015; Davidzon et al. 2017; Wright et al. 2018). The higher amplitude of their GSMF is attributed to differences in the SED fitting assumptions, where their method produces systematically older stellar ages and higher stellar masses than in previous studies.

Here we present a new analysis of the massive portion of the $z \approx 0$ GSMF at $M_* \gtrsim 3 \times 10^{11} \, M_\odot$, a regime of considerable debate. Several GSMF studies examined in Leja et al. (2020) do not sample a large enough local volume to have sufficient statistics for determining this part of the GSMF. The exceptions are analyses based on galaxies in the Sloan Digital Sky Survey (SDSS; e.g., Li & White 2009; Bernardi et al. 2013; Moustakas et al. 2013; D'Souza et al. 2015). But the large spatial extents and faint outer envelopes of the local massive galaxies have made it challenging to obtain accurate sky subtraction, surface brightness profile fitting, and total luminosity (and hence stellar mass). Bernardi et al. (2013) find that the number density of high-mass SDSS galaxies is highly dependent on the photometric fitting scheme used to measure the total light. D'Souza et al. (2015) estimate a series of flux corrections by stacking images of similar galaxies, finding that the SDSS `model` magnitudes underrepresent the brightness of the most massive galaxies in their sample by up to 0.4 mag. With these changes, D'Souza et al. (2015) find the number density of $M_* \sim 5 \times 10^{11} \, M_\odot$ galaxies to be a factor of ∼3 lower than Bernardi et al. (2013) and a factor of ∼6 higher than Li & White (2009), even though the three analyses all rely on SDSS observations. Furthermore, none of these studies explore variations in the stellar initial mass function (IMF) and instead assume a Milky Way IMF.

Reducing the uncertainties in the local GSMF at high masses has far-reaching implications. One example is the puzzling lack

of net evolution in the massive end of the GSMF between $z \sim 1$ and 0 reported in a number of studies (Moustakas et al. 2013; Bundy et al. 2017; Leja et al. 2020, and references therein). A nonevolving GSMF over this redshift range implies that massive galaxies have experienced little mass gain in the past ~ 8 billion yr, in contrast to the mass growth through galaxy mergers expected since $z \sim 1$. Another potential puzzle related to the local galaxy and SMBH populations is whether the predicted and detected amplitudes of the stochastic gravitational-wave background in the nanohertz regime are consistent with each other. A recent analysis indicates that the amplitudes reported by various Pulsar Timing Array (PTA) teams (NANOGrav, Agazie et al. 2023a; the European PTA and Indian PTA, EPTA Collaboration et al. 2023; and the Parkes PTA, Reardon et al. 2023), if originated from merging SMBH binaries, would imply a much higher space density of local massive SMBHs than observed (Sato-Polito et al. 2023). A key link in the models used to predict the gravitational-wave amplitude is the local GSMF (or related galaxy velocity dispersion function, VDF). Another consideration is how the GSMF is related to the BHMF inferred from different SMBH populations at various redshifts (e.g., local quiescent versus high-z active) and the implications for the mass accretion histories of SMBHs (e.g., Shankar et al. 2004; Kelly & Merloni 2012).

Here we incorporate results from the MASSIVE survey (Ma et al. 2014) in an analysis of the high-mass portion of the local GSMF and the associated BHMF. MASSIVE is a volume-limited multiwavelength imaging and spectroscopic survey of ~ 100 galaxies in the northern sky (decl. $\delta > -6°$), targeting all early-type galaxies with $M_* \gtrsim 5 \times 10^{11}\ M_\odot$ to a distance of 108 Mpc. Spatially resolved stellar kinematics of MASSIVE galaxies have been obtained from extensive sets of integral-field spectroscopic observations (Veale et al. 2017a, 2017b, 2018; Ene et al. 2018, 2019, 2020). Hubble Space Telescope (HST) observations of a subset of MASSIVE galaxies and deep K-band observations of the majority of the galaxies with WIRCam on the Canada–France–Hawaii Telescope (CFHT) have also been acquired (Goullaud et al. 2018; Quenneville et al. 2024). Together, these data sets enable in-depth dynamical modeling to be performed to determine the spatial mass distributions of the stars and dark matter within a galaxy and the mass of the central SMBH. In addition, deep long-slit spectroscopic observations covering 4000–10300 Å have been conducted to measure the spatial gradients of chemical abundances, IMFs, and stellar mass-to-light ratios for a sample of MASSIVE galaxies using stellar population synthesis (SPS) modeling (Gu et al. 2022). These dynamical and SPS measurements of M_* enable us to perform a new assessment of the local high-mass GSMF that is independent of the SED fitting methods used to convert stellar light to mass.

In Section 2, we discuss the available sets of dynamical M_* and SPS M_* for MASSIVE galaxies. A list of MASSIVE galaxies with dynamical masses from stellar orbit modeling, stellar Jeans modeling, or gas kinematics is provided in Table A1. We derive a scaling relation between each set of M_* and the K-band absolute magnitudes, M_K, considering M_K from both Two Micron All Sky Survey (2MASS; Skrutskie et al. 2006) and deeper CFHT observations (Section 2.3). This relation is then used to infer the stellar mass distribution for the entire MASSIVE sample (Section 2.4). In Section 3, a $z = 0$ GSMF is constructed to reproduce the result of Leja et al.

(2020) for $M_* \lesssim 10^{11.3}\ M_\odot$ and the MASSIVE measurements at $M_* \gtrsim 10^{11.5}\ M_\odot$. In Section 4, we convolve our GSMF and several GSMFs from the literature with the scaling relation between galaxy mass and SMBH mass to obtain the local BHMF and to estimate the number of massive SMBHs in the local volume. In Section 5, we calculate the amplitude of the gravitational waves in the nanohertz range due to the cosmological distribution of merging SMBHs from each BHMF and compare it with the PTA results. The $z = 0$ SMBH mass density from integration of each BHMF is discussed.

2. Stellar Mass of Local Massive Early-type Galaxies

When the MASSIVE survey was planned (Ma et al. 2014), the target galaxies were selected based on stellar masses inferred from the 2MASS absolute K-band magnitudes and Equation (2) of Cappellari (2013): $\log_{10}(M_*/M_\odot) = 10.58 - 0.44(M_K^{2MASS} + 23)$. This empirical formula is a fit to the 2MASS M_K of galaxies in the ATLAS^{3D} survey (Cappellari et al. 2011) and dynamical masses determined from Jeans modeling (assuming no dark matter). By design, however, there is little overlap in the galaxy mass range probed by the two surveys. The ATLAS^{3D} survey targets lower-mass early-type galaxies ($M_* \gtrsim 10^{10}\ M_\odot$) in a smaller volume (to a distance of 42 Mpc); only six galaxies in that sample are massive enough to make it into the MASSIVE survey. While their M_*–M_K relation used the best available information at that time, its validity for M_* above $\sim 10^{11.5}\ M_\odot$, or $M_K \sim -25$ mag, is untested. There is now a sample of MASSIVE galaxies with dynamical or SPS stellar masses for us to calibrate the relationship between M_K and M_* at high masses.

2.1. Stellar Mass from Dynamical Modeling

In Table A1, we compile a list of MASSIVE galaxies for which dynamical modeling has been performed using detailed spectroscopic measurements of stellar or gas velocities as constraints. Some of these galaxies have been studied with multiple dynamical modeling methods or tracers. In the case of stellar dynamics, 11 galaxies have been modeled with the Schwarzschild orbit method using spatially resolved stellar kinematics, assuming either an axisymmetric or triaxial potential. All three major mass components in the galaxies—SMBH, stars, and dark matter—are included in these orbit models, so we have a direct inference of the dynamical mass of the stellar component of each galaxy. The dark matter halo in each case is parameterized by a standard form (e.g., logarithmic or Navarro–Frenk–White). The dark matter fraction within R_e (when reported and when R_e is well determined) ranges from $\sim 15\%$ to 40%.

We note a few caveats to some of the measurements in Table A1. The Jeans stellar dynamical modeling of NGC 5322, NGC 5353, NGC 5557, and NGC 7052 uses a single mass component (Cappellari et al. 2013), so there is no mass measurement of the stellar component that can be compared fairly with M_* from the orbit method for other galaxies. The CO gas dynamics of NGC 997 and NGC 1684 probe only the inner ~ 2 kpc of the galaxies and do not directly constrain the stellar mass beyond this region (Dominiak et al. 2024).

2.2. Stellar Mass from SPS Modeling

Gu et al. ([2022](#)) present a comprehensive SPS study of 41 MASSIVE galaxies and measurements of their chemical abundances, stellar IMFs, and stellar mass-to-light ratios. The high signal-to-noise ratio (S/N) spectra are obtained from deep spectroscopic observations with LDSS-3 on the Magellan Telescope, covering the spectral range of 4000–10300 Å. The mean S/N level (per angstrom) is 120 in the blue and 230 in the red. Since the MASSIVE galaxies are selected to have a decl. above $-6°$, only this subset of 41 galaxies are suitable for observations with Magellan.

Table A1 (column (5)) of Gu et al. ([2022](#)) lists the total M_* from SPS modeling. These values are obtained from the luminosity-weighted r-band M_*/L_r within the effective radius, R_e, in their SPS model and the total L_r from the Siena Galaxy Atlas (Moustakas et al. [2021](#), [2023](#)), where available, or from SDSS. The total galaxy magnitudes from Siena are in the SDSS r band and estimated using the curve-of-growth method. For consistency with the K-band measurements used in this Letter, we instead use M_*/L_K (again, luminosity weighted within R_e) from the same data and SPS models (M. Gu et al. 2024, in preparation) and multiply it by L_K from deep K-band CFHT observations (see below) to obtain the SPS-based M_*.

We find the two sets of SPS mass-to-light ratios, M_*/L_r and M_*/L_K, to be well related by a mean color of $r - K = 2.74$, a value consistent with expectations for a 10 Gyr old stellar population with slightly above solar metallicity (Vazdekis et al. [2012](#)). When the Siena L_r is shifted by this mean color, we find a residual 0.25 mag difference from the CFHT L_K; that is, the Siena luminosities are on average 20% smaller than those from CFHT. This residual difference could be due to differences in the depths of the two surveys, differences in the methods used to determine L, or uncertainties in SPS modeling.

2.3. The M_*–M_K Relation

We now examine the correlation between M_K and stellar masses determined by either dynamical or SPS modeling discussed above in the form of

$$\log_{10}(M_*/M_\odot) = \alpha - \beta(M_K + 26). \quad (1)$$

We consider two sets of measurements of M_K in this analysis: the original 2MASS values, M_K^{2MASS}, from Ma et al. ([2014](#)) and the updated values, M_K^{CFHT}, from the homogeneous deep K-band observations with WIRCam on the CFHT from Quenneville et al. ([2024](#)). The M_K^{2MASS} values are obtained from the 2MASS apparent K-band magnitudes and distances compiled in Ma et al. ([2014](#)). These measurements are useful for a direct comparison with the M_*–M_K relation in Equation (2) of Cappellari ([2013](#)), which is also based on the 2MASS K-band photometry. To improve on the shallow 2MASS photometry, the MASSIVE team has conducted deep CFHT K-band observations, reaching 2.5 mag deeper than 2MASS to capture the outer envelopes of these massive galaxies (Quenneville et al. [2024](#)). In that work, a nonparametric curve-of-growth method is used to determine the total magnitude of each galaxy; the results therefore do not rely on assuming a particular functional form for the surface brightness profiles, as is frequently done in prior work. The apparent K magnitudes from CFHT are found to be brighter than 2MASS by 0.292 mag on average (see their Figure 2). A complete list of

K^{2MASS} and K^{CFHT} are given in Table A1 of Quenneville et al. ([2024](#)).

2.3.1. Dynamical M_* versus M_K^{2MASS}

We first examine the correlation between M_K^{2MASS} and dynamically determined M_* in Section [2.1](#), as displayed in Figure [1](#) (left panel). For uniformity, we include only the galaxies in which the stars and dark matter have been reliably modeled as separate components (filled circles). Individual measurement errors are estimated to be 0.1 mag in M_K (Skrutskie et al. [2006](#); Quenneville et al. [2024](#)), and the formal errors on M_* from dynamical modeling tend to be small (e.g., 3.5% for NGC 1453 in Quenneville et al. [2022](#) and <1% for NGC 315 in Boizelle et al. [2021](#)). We adopt a uniform error of 0.1 dex on each M_* value to incorporate systematic uncertainties. We find M_* and M_K^{2MASS} to be well approximated by Equation ([1](#)) with $\alpha = 11.92 \pm 0.06$ and $\beta = 0.49 \pm 0.16$; the intrinsic scatter is 0.16 dex (gray line and shaded region). This relationship is empirically determined over the magnitude range represented by MASSIVE galaxies. The dominant source of uncertainty in the inferred stellar masses is the intrinsic scatter in the relationship, but if the relationship is extrapolated to substantially fainter magnitudes, the uncertainty in the slope β will be dominant.

Since both M_K and M_* depend on the distance assumed for a galaxy, we ensure that the same distance is used for the two quantities when deriving the M_*–M_K relation. The distances used to evaluate M_K^{2MASS} were assigned as follows (see Section 2.2 of Ma et al. [2014](#) for details): for galaxies that belong to groups in the 2MASS Galaxy Redshift Catalog (2MRS; Crook et al. [2007](#); Huchra et al. [2012](#)), local peculiar velocities were removed and group-corrected redshift distances were assigned; for isolated galaxies with no identifiable groups, redshift distances were assigned based on radial velocities corrected with flow models. We adopt these distances here (column (2) of Table [A1](#)). If a different distance was assumed in the relevant dynamical modeling work (column (4)), we scale their M_* using the ratio of the distances in columns (2) and (4) in Table [A1](#).

Our relation between dynamical M_* and M_K^{2MASS} has a slightly steeper slope than the relation of Cappellari ([2013](#)) and yields a ~10% higher M_* at a fixed M_K^{2MASS}. The actual difference, however, is larger because only a single mass component is modeled in Cappellari ([2013](#)), so their reported dynamical masses are upper limits on the true stellar masses.

2.3.2. Dynamical M_* versus M_K^{CFHT}

For the relation between M_K^{CFHT} and dynamically determined M_*, we find it well fit by Equation ([1](#)) with $\alpha = 11.85 \pm 0.06$, $\beta = 0.43 \pm 0.13$, and an intrinsic scatter of 0.16 dex, as indicated by the blue line and shaded region in the middle panel of Figure [1](#).

As in the previous section, we have ensured that the same distance is used in evaluating M_* and M_K^{CFHT} for each galaxy. For uniformity, we adopt the distances used to obtain M_K^{CFHT} in Quenneville et al. ([2024](#)). For the galaxies with reliably dynamical M_* considered here, the distances have all been measured recently with the surface brightness fluctuation (SBF) method (Blakeslee et al. [2021](#); Jensen et al. [2021](#)) and are listed in column (3) of Table [A1](#). We scale each M_* from the
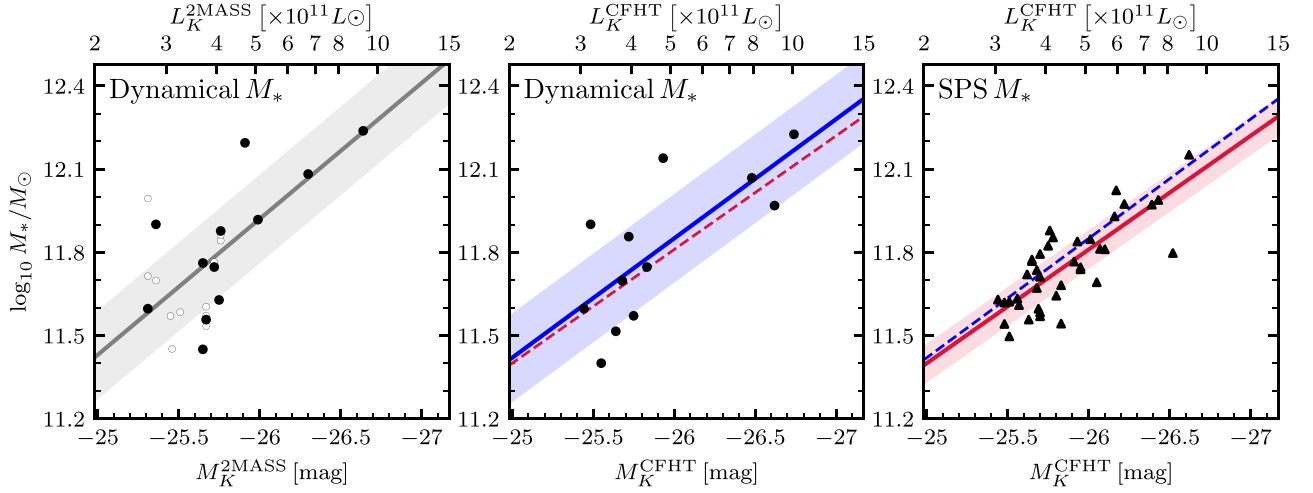
Figure 1. Stellar mass M_* vs. absolute K-band magnitude M_K of MASSIVE galaxies with M_* measurements from dynamical modeling (left and middle) or SPS modeling (right). For dynamical M_*, two sets of M_K are shown: 2MASS (left) and CFHT (middle). The solid line in each panel represents the respective best-fitting relation (from left to right): $\log_{10}(M_*/M_\odot) = 11.92 - 0.49(M_K^{2MASS} + 26)$, $\log_{10}(M_*/M_\odot) = 11.85 - 0.43(M_K^{CFHT} + 26)$, and $\log_{10}(M_*/M_\odot) = 11.81 - 0.41(M_K^{CFHT} + 26)$; each shaded band indicates the intrinsic scatter. Filled symbols indicate the measurements used in each fit. Open circles in the left panel mark either multiple M_* measurements of the same galaxy from other methods not used in the fit or systems excluded from the fit (see Section 2.1 and Table A1). For ease of comparison, the best-fit blue line in the middle panel is shown as a dashed blue line in the right panel, and similarly for the red lines, illustrating that SPS M_* is on average $\sim$7% lower than dynamical M_*.

literature by the ratio of the distances in columns (3) and (4); the adjusted M_* are tabulated in column (8).

While the deeper CFHT observations yield brighter K-band magnitudes than 2MASS on average (by 0.292 mag, or a 31% increase in luminosity), because the new SBF distances are on average smaller, the M_K^{CFHT} in Figure 1 is on average 0.12 mag brighter than M_K^{2MASS}.

2.3.3. SPS M_* versus M_K^{CFHT}

We repeat the analysis in the last subsection using the SPS M_* discussed in Section 2.2. The SPS M_* and M_K^{CFHT} for the 41 galaxies in the Gu et al. (2022) sample are displayed in the right panel of Figure 1. The best-fitting relation is given by Equation (1) with $\alpha = 11.81 \pm 0.02$ and $\beta = 0.41 \pm 0.05$; the intrinsic scatter is 0.07 dex (red line and shaded region). The dynamical M_* and M_K^{CFHT} relation is plotted as a dashed blue line for comparison. The two independent methods used to infer M_* agree well, with the SPS M_* on average $\sim$7% smaller than the dynamical M_*.

2.4. Stellar Mass Distribution of the MASSIVE Sample

Having established the M_*–M_K relation using the subset of MASSIVE galaxies with existing dynamical or SPS M_* in the previous sections, we can now use M_K as a proxy and apply the relation to estimate M_* for the MASSIVE galaxies without these detailed measurements. The distribution of M_* based on each of the three versions of the relation is shown in Figure 2. The two distributions of dynamical-based M_* inferred from M_K^{CFHT} (blue curve) and M_K^{2MASS} (gray curve) agree well. This is expected because the two $M_* - M_K$ relations are both calibrated to MASSIVE galaxies with reliable dynamical M_*. The distribution of SPS-based M_* (red curve) is lower than that of dynamical-based M_* (blue curve) because the SPS M_* is on average 7% lower (see Section 2.3.3). Since the CFHT observations more accurately capture the galaxies' total luminosities than the 2MASS observations, we will use the

SPS and dynamical M_* inferred from M_K^{CFHT} in the subsequent analysis.

As a final remark, we note that when M_K^{CFHT} is used to estimate either the SPS or dynamical M_* above, we need to first homogenize the distance measurements. This step is necessary because even though the galaxies used to calibrate the $M_* - M_K^{CFHT}$ relation all happen to have SBF distances, SBF distances are available for only $\sim$40% of the whole MASSIVE sample. For this 40% of galaxies, we find the SBF distances to be 93% $\pm$ 12% of the 2MRS distances compiled in Ma et al. (2014). To avoid introducing systematic biases in MASSIVE galaxies without SBF measurements, we apply this correction factor to the original distances in Ma et al. (2014) and use the SBF-like distances to obtain M_K^{CFHT}. While careful handling of the assumed distance is important for improving the accuracy of each individual stellar mass measurement, the random errors associated with the distance ($\sim$10%) are small compared to the intrinsic scatter we found in the $M_* - M_K$ relations in Section 2.3.

3. The Stellar Mass Function at $z = 0$

In this section, we construct a $z = 0$ GSMF that both reproduces the GSMF of Leja et al. (2020) below $M_* \sim 10^{11} M_\odot$ and matches the local measurements based on the volume-limited MASSIVE survey at $M_* \gtrsim 10^{11.5} M_\odot$ (Ma et al. 2014; Gu et al. 2022; Quenneville et al. 2024). A flat ΛCDM cosmology with $\Omega_m = 0.3$ and $H_0 = 70$ km s^{-1} Mpc^{-1} is assumed.

3.1. Survey Volume

To convert the stellar mass distribution of MASSIVE galaxies in Figure 2 into a mass function, we first estimate the volume surveyed by MASSIVE. To do so, we recall that MASSIVE is primarily a northern-sky survey, targeting all early-type galaxies in the 2MASS catalog satisfying (i) geometric cuts of distance $D < 108$ Mpc and decl. $\delta > -6°$, (ii) absolute magnitude cuts of $M_K^{2MASS} < -25.3$ mag, and (iii) extinction cuts of $A_V < 0.6$ in
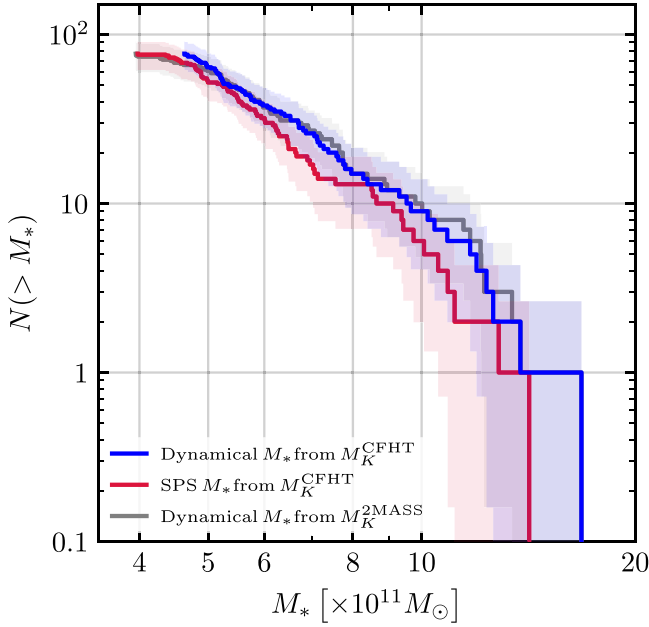
Figure 2. Number of MASSIVE galaxies above stellar mass M_*. Each histogram is for M_* from the corresponding M_*–M_K relation in Figure 1; when available, the dynamical or SPS M_* values are used instead of M_* from the scaling relation. The blue and gray curves are very similar because both are calibrated to MASSIVE galaxies with reliable dynamical M_*. The red curve has a lower amplitude because the SPS M_* is on average ∼7% lower than the dynamical M_*. Each shaded band represents the 90% confidence region.

the Extended Source Catalog (XSC; Jarrett et al. 2000) of 2MASS.

MASSIVE covers 55% of the sky before the extinction cuts. To estimate the effect of extinction on the survey's sky coverage, we generate a large number of test points uniformly distributed in solid angle with $\delta > -6°$ and then apply the same extinction and reddening relations (Fitzpatrick 1999; Schlafly & Finkbeiner 2011) used in the MASSIVE survey to each point. About 76% of the points pass the extinction cut of $A_V < 0.6$. MASSIVE therefore effectively covers 41.9% of the whole sky, or ∼17,280 deg². Folding in the distance cut, we estimate the comoving survey volume of MASSIVE to be $2.05 × 10^6$ Mpc³. A simple geometric volume of $\frac{4\pi}{3}(0.419)(108 \text{ Mpc})^3 = 2.21 × 10^6$ Mpc³ would lead to an overestimate of 8%. The primary source of uncertainty in the survey volume is the assumed distance cut. When computing the GSMF in the next section, we use the differential comoving volume associated with each galaxy's measured distance as a normalization factor rather than assuming a single total survey volume.

For comparison, the sky coverage of the COSMOS-2015 and 3D-HST catalogs used in Leja et al. (2020) is ∼2 deg² and ∼0.25 deg², respectively. These deep surveys are designed to probe galaxy evolution over a wide redshift range beyond the local volume. The volume covered by these surveys within the distance cut of MASSIVE is tiny in comparison to that of MASSIVE: 237 Mpc³ for COSMOS-2015 and 29.7 Mpc³ for 3D-HST. To ensure a reasonable sample size, Leja et al. (2020) limit their GSMF determination to $z > 0.2$ and $z > 0.5$ for the two surveys, respectively.

3.2. Stellar Mass Function and Schechter Form

To incorporate the GSMF from Leja et al. (2020), we first make a minor adjustment and extrapolate their $z = 0.2$ GSMF

(the lowest redshift presented there) to $z = 0$. This is achieved using the procedure in their Appendix B. This adjustment results in little change at $M_* \gtrsim 10^{11.25} M_\odot$, about an 8% increase in the amplitude at $M_* \sim 10^{11} M_\odot$, and about a 15% increase at $M_* \lesssim 10^{10.5} M_\odot$. The resulting GSMF is plotted as a green dashed curve in the top panel of Figure 3. Since the 3D-HST and COSMOS-2015 surveys contain few galaxies above $M_* \sim 10^{11} M_\odot$ in the local volume (Figure 1 of Leja et al. 2020), we include only the $M_* < 10^{11} M_\odot$ portion of their GSMF in the analysis below.

We find the combined GSMF from MASSIVE and Leja et al. (2020) to be well approximated as a sum of two Schechter functions,

$$\frac{dn}{d\ln M_*} = \left[\phi_1\left(\frac{M_*}{M_s}\right)^{\alpha_1+1} + \phi_2\left(\frac{M_*}{M_s}\right)^{\alpha_2+1}\right]e^{-\left(\frac{M_*}{M_s}\right)^\beta}, \quad (2)$$

where we assume the same scale mass M_s for the two components and $\beta = 1$ as in Leja et al. (2020). We assign the more negative slope to α_2 so that the second term is dominant at low masses, while the first term is dominant at high masses. We compute posteriors on the five parameters (ϕ_1, ϕ_2, α_1, α_2, M_s) in Equation (2) with dynamic nested sampling using dynesty (Speagle 2020) and list the results in Table B1. This procedure is performed twice, once using MASSIVE dynamically inferred M_* and once using MASSIVE SPS inferred M_*, i.e., the blue and red distributions in Figure 2, respectively. We use a combined posterior from the average of these two posteriors to obtain our fiducial GSMF. Details of the GSMF fitting procedure and instructions for how to generate the posterior distribution are provided in Appendix B.

The resulting $z = 0$ GSMF is shown as a violet band in the top panel of Figure 3. The median GSMFs from the separate fits to the dynamical and SPS M_* of MASSIVE galaxies are represented by the blue and red curves, respectively. By design, our GSMFs reproduce the $z = 0$ GSMF of Leja et al. (2020; green dashed curves) at $M_* \lesssim 10^{11} M_\odot$. For comparison, three additional GSMFs from prior studies of $z \sim 0$ SDSS galaxies are plotted (Bernardi et al. 2013; Moustakas et al. 2013; D'Souza et al. 2015). The three GSMFs roughly agree at lower masses but start to differ above $M_* \sim 10^{11} M_\odot$. Bernardi et al. (2013) and D'Souza et al. (2015) both adopt improved SDSS magnitude measurements but with different approaches. The two GSMFs agree well at lower masses, but D'Souza et al. (2015) is a factor of ∼8 lower at $M_* \sim 10^{12} M_\odot$. Moustakas et al. (2013) do not correct the SDSS magnitudes and instead use stellar masses from the NYU-VAGC catalog (Blanton et al. 2005). Their GSMF is a factor of ∼3 lower than D'Souza et al. (2015) above $M_* \sim 10^{11.5} M_\odot$.

Figure 3 shows that our GSMF (violet band) has a higher amplitude at high masses than the four studies discussed above (dashed curves). It is instructive to compare the number of galaxies expected from each GSMF within the MASSIVE survey volume, which is plotted in the bottom panel of Figure 3. The GSMF of Bernardi et al. (2013) would predict a factor of ∼2 lower number than the actual galaxy counts in MASSIVE. Moustakas et al. (2013), D'Souza et al. (2015), and Leja et al. (2020) would predict even fewer massive galaxies in this volume, from zero to ∼10 galaxies with $M_* \gtrsim 5 × 10^{11} M_\odot$, a large discrepancy from the ∼100 galaxies in the MASSIVE survey.

4. The BHMF at $z = 0$

4.1. BHMFs Derived from Galaxy Distributions

We use established black hole and galaxy bulge mass scaling relations to convert the GSMF in the previous section into a BHMF. This is achieved by convolution between the GSMF and a probability distribution function associated with the $M_{BH}-M_*$ scaling relation: $\log_{10}(M_{BH}/M_\odot) = (8.46 \pm 0.08) + (1.05 \pm 0.11)\log_{10}(M_\star/10^{11}M_\odot)$ from McConnell & Ma (2013). This relation assumes lognormal scatter in M_{BH} at a given galaxy mass, so we use the lognormal probability distribution function as the kernel of the convolution. We find that the results are essentially unchanged if the scaling relation of Saglia et al. (2016) is used.

The BHMF derived from our GSMF is displayed as a violet band (90% confidence interval) in the top panel of Figure 4. The width of the band arises predominantly from the intrinsic scatter of 0.34 dex in the $M_{BH}-M_*$ scaling relation. We find this BHMF to be well approximated by a single Schechter function of the form

$$\frac{dn}{d\ln M_{BH}} = \phi\left(\frac{M_{BH}}{M_s}\right)^{\alpha+1} e^{-\left(\frac{M_{BH}}{M_s}\right)^\beta}, \qquad (3)$$

where $\alpha = -1.27 \pm 0.02$, $\beta = 0.45 \pm 0.02$, $\log_{10}(\phi/\text{Mpc}^{-3}) = -2.00 \pm 0.07$, and $\log_{10}(M_s/M_\odot) = 8.09 \pm 0.09$.

The BHMFs derived from the GSMFs of Bernardi et al. (2013), D'Souza et al. (2015), and Leja et al. (2020) are plotted as dashed curves for comparison. The uncertainties in these BHMFs (not shown for clarity) are comparable to the violet band because the scatter in the $M_{BH}-M_*$ relation is the dominant source of uncertainty. The BHMF inferred from Bernardi et al. (2013) is consistent with the 90% error band of our BHMF. The lower amplitudes of the GSMFs of D'Souza et al. (2015) and Leja et al. (2020) at $M_* \gtrsim 10^{11.3} M_\odot$ result in lower amplitudes in the BHMFs at $M_{BH} \gtrsim 10^9 M_\odot$.

For further comparison, we include the BHMF (cyan dotted–dashed curve) based on the galaxy VDF and the $M_{BH}-\sigma$ scaling relation used in Sato-Polito et al. (2023). The VDF is from Bernardi et al. (2010), and the $M_{BH}-\sigma$ relation is from McConnell & Ma (2013). This σ-based BHMF overlaps with our BHMF at $M_{BH} \gtrsim 3 \times 10^9 M_\odot$, but at lower M_{BH}, it predicts a significantly lower number density than any M_*-based BHMF shown in Figure 4. A similar inconsistency is reported in Lauer et al. (2007), who find more SMBHs above $10^9 M_\odot$ when galaxy luminosities instead of σ are used as the proxy for M_{BH}.

As a final comparison, we plot the BHMF (cyan dotted curve) based on the same VDF but with the hypothetical double power-law $M_{BH}-\sigma$ relation proposed in Sato-Polito et al. (2023). The authors introduce a much steeper second power law in this ad hoc $M_{BH}-\sigma$ relation in order to match the amplitude of the stochastic gravitational-wave background observed by PTA teams. As pointed out in that work, this BHMF would predict significantly more SMBHs above $M_{BH} \sim 10^9 M_\odot$ than if the standard single power-law $M_{BH}-\sigma$ relation were used (cyan dotted–dashed curve). This BHMF also far exceeds our M_*-based BHMF at $M_{BH} \gtrsim 10^{10.3} M_\odot$ (violet band). We will discuss the implications below.
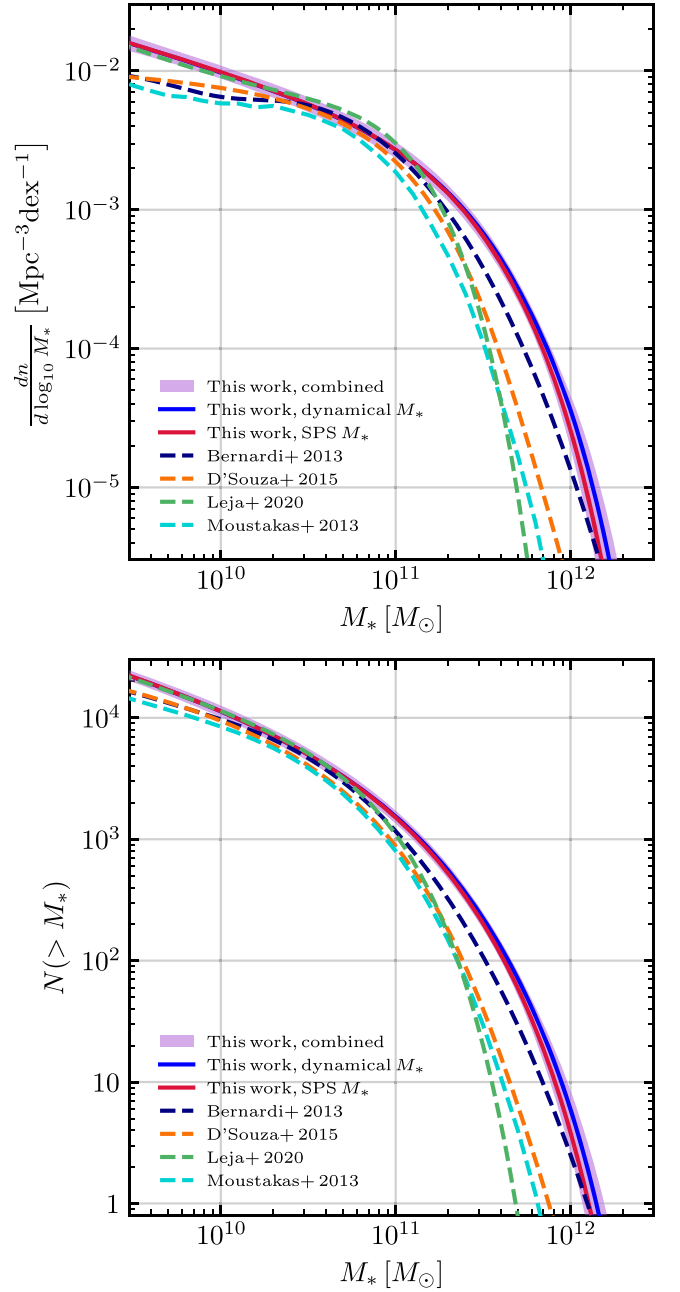

Figure 3. (Top) The $z = 0$ GSMF from this Letter (violet band; 90% confidence interval). It is constructed to reproduce the $z = 0$ GSMF of Leja et al. (2020; green dashed curve) at $M_* \lesssim 10^{11} M_\odot$ and to match the stellar mass distribution of MASSIVE galaxies at $M_* \gtrsim 10^{11.5} M_\odot$. The violet band represents the GSMF from averaging two separate posterior distributions for MASSIVE dynamically inferred M_* (blue curve) and SPS inferred M_* (red curve). Three GSMFs from prior studies of SDSS galaxies are shown for comparison: Bernardi et al. (2013; indigo), D'Souza et al. (2015; orange), and Moustakas et al. (2013; cyan). (Bottom) Cumulative galaxy counts in the MASSIVE survey volume estimated from each GSMF in the top panel. The orange, green, and cyan curves would yield fewer than 10 galaxies in the MASSIVE survey.

4.2. How Many Big Black Holes Are There?

To estimate the expected number of SMBHs above mass M_{BH} in the local Universe, we integrate each $z = 0$ BHMF discussed above and multiply by the MASSIVE survey volume. The resulting number distributions of $M_{BH} > 10^9 M_\odot$ SMBHs are shown in the bottom panel of Figure 4. To compare with known
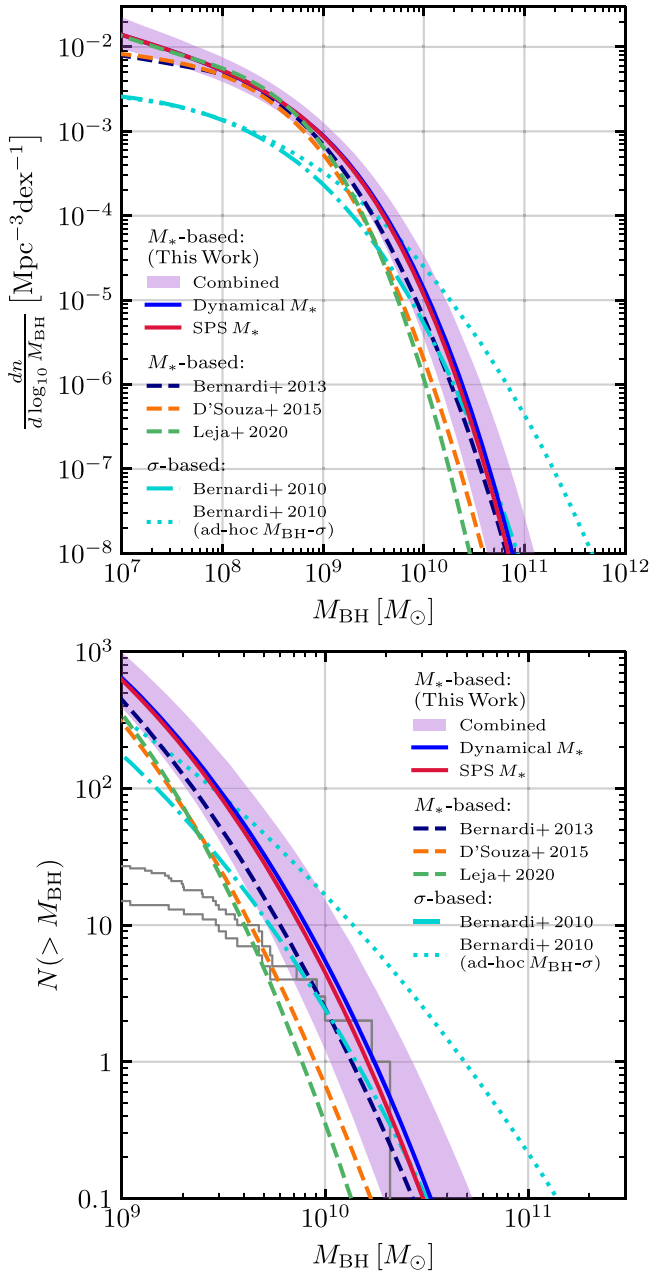
Figure 4. (Top) The $z = 0$ BHMF inferred from our GSMF and the M_{BH}–M_* scaling relation (violet band; 90% confidence interval). The dashed curves represent the BHMFs computed from the other GSMFs in Figure 3. The two cyan curves compare the BHMFs inferred from the galaxy VDF instead of the GSMF using the standard M_{BH}–σ relation (dotted–dashed) vs. the ad hoc M_{BH}–σ relation (dotted) from Sato-Polito et al. (2023). (Bottom) The SMBH number counts (above mass M_{BH}) within the MASSIVE survey volume predicted by each BHMF in the top panel. The gray histograms compare the counts of dynamically detected SMBHs within 108 Mpc (top for the entire sphere; bottom for the northern portion surveyed by MASSIVE).

SMBHs, we compile a list of SMBHs with dynamically determined masses above $10^9\,M_\odot$ out to the MASSIVE survey distance (108 Mpc) and plot the mass distribution as gray histograms (top for the entire sphere; bottom for the northern portion surveyed by MASSIVE). This list is based on the samples from McConnell et al. (2013) and Saglia et al. (2016) and new SMBHs in this mass range and volume reported since those compilations (Walsh et al. 2015, 2016, 2017; Thomas et al. 2016; Boizelle et al. 2021; Pilawa et al. 2022; Quenneville et al.

2022; Liepold et al. 2023; de Nicola et al. 2024; Dominiak et al. 2024; Mehrgan et al. 2024).

The BHMF based on the GSMF proposed in this Letter (violet band) predicts 1–14 (90% confidence interval) SMBHs with $M_{BH} \gtrsim 10^{10}\,M_\odot$ and between 0.1 and 2.2 at $M_{BH} \gtrsim 2 \times 10^{10}\,M_\odot$, consistent with the known number of SMBHs in this mass range. In comparison, the cyan dotted curve proposed in Sato-Polito et al. (2023) predicts many more ultramassive SMBHs than observed.

Another noteworthy feature of the bottom panel of Figure 4 is that all curves predict many more $M_{BH} \sim 10^9\,M_\odot$ SMBHs than currently known. This is a reflection of the incomplete census of local SMBHs. Direct dynamical inference of an SMBH and a robust measurement of its mass require time-consuming observational and modeling efforts. Among the most massive $\sim$100 local galaxies targeted by the MASSIVE survey, only $\sim$15 SMBHs have been inferred from detailed dynamical methods thus far (Table A1). Ongoing efforts are expected to increase this sample.

5. Implications

5.1. Amplitude of Stochastic Gravitational Waves

The cosmological distribution of merging SMBH binaries is expected to produce a stochastic gravitational-wave background with a characteristic spectrum and amplitude that depend on the properties of the mergers. Consider an SMBH binary at redshift z with a mass ratio $q = M_2/M_1 \leqslant 1$, total mass $M = M_1 + M_2$, and chirp mass $\mathcal{M}$, where $\mathcal{M}^{5/3} = M^{5/3}q/(1 + q)^2$. The distribution of these binaries is represented by the mass function $d^3n(M, q, z)/dM\,dq\,dz$, which defines the differential number density of binaries with M, q, and z. For SMBH binaries on circular orbits where the orbital decay is purely driven by gravitational radiation, the characteristic amplitude of the gravitational waves at frequency f (over interval $d\ln f$) can be written as (Phinney 2001)

$$h_c^2(f) = \frac{4\pi}{3c^2}\frac{1}{(\pi f)^{4/3}}$$
$$\times \int dM\,dq\,dz\,\frac{d^3n}{dM\,dq\,dz}\frac{q(GM)^{5/3}}{(1 + q)^2}\frac{1}{(1 + z)^{1/3}}. \tag{4}$$

Sato-Polito et al. (2023) further assume that the distributions in M, q, and z are separable and replace $d^3n/dM\,dq\,dz$ with $p_z(z)p_q(q)dn/dM$, where $p_z(z)$ and $p_q(q)$ are the normalized distributions of redshifts and mass ratios, respectively. They also assume that each present-day SMBH has experienced a single merger in its lifetime and identify dn/dM as the local BHMF with $M = M_{BH}$. The strain is then simplified to

$$h_c^2(f) = \frac{4\pi}{3c^2}\frac{1}{(\pi f)^{4/3}}\langle q/(1 + q)^2\rangle\langle(1 + z)^{-1/3}\rangle$$
$$\times \int dM\frac{dn}{dM}(GM)^{5/3}$$
$$= 1.18 \times 10^{-30}\left(\frac{yr^{-1}}{f}\right)^{4/3}\langle q/(1 + q)^2\rangle\langle(1 + z)^{-1/3}\rangle$$
$$\times \int dM\left(\frac{M}{10^9 M_\odot}\right)^{5/3}\frac{d}{dM}\left(\frac{n}{10^{-4}\mathrm{Mpc}^{-3}}\right), \tag{5}$$
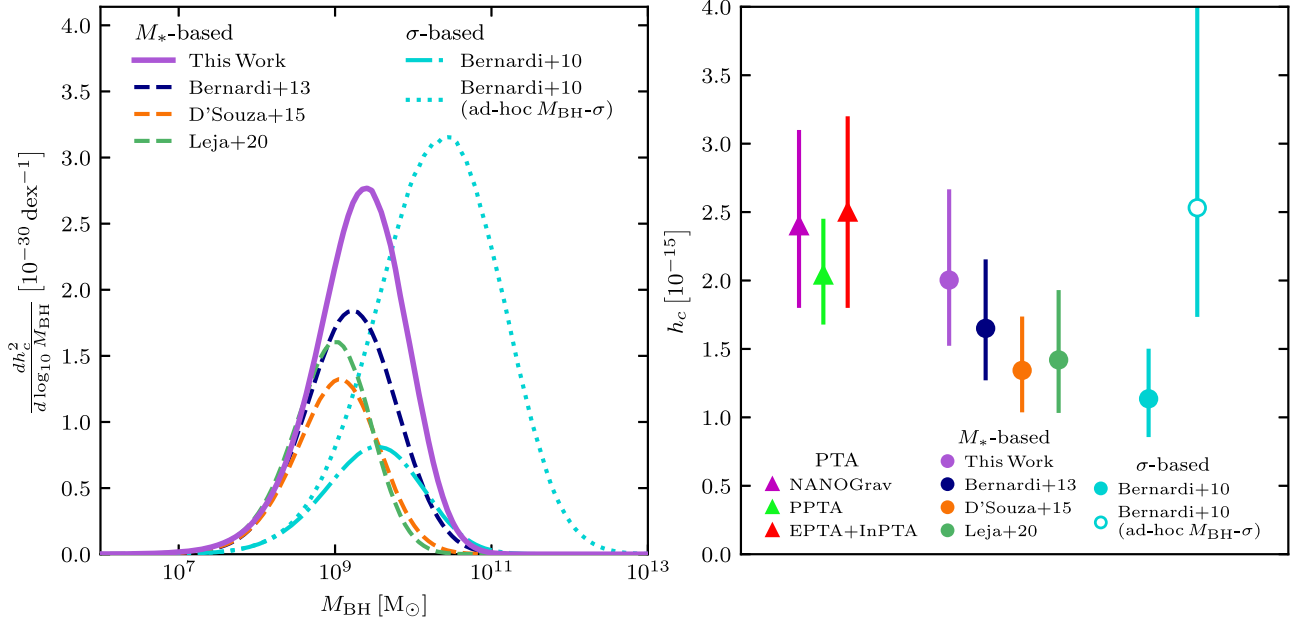
Figure 5. Comparison of the characteristic amplitude of gravitational waves at $f = 1\,\mathrm{yr}^{-1}$, h_c, reported by the PTA teams and predicted by BHMFs inferred from galaxy distribution functions. The right panel shows h_c, and the left panel shows the differential contribution to h_c^2, $dh_c^2/d\log_{10}M_{\mathrm{BH}}$, as a function of M_{BH}. The predicted amplitudes are computed from Equation (5) using the BHMFs in Figure 4. All error bars denote 90% confidence intervals. The published PPTA value quotes a 68% interval; we enlarge it by a factor of 1.64 to approximate the 90% interval. The individual value of h_c (in units of 10^{-15}) is (from left to right): $(2.4^{+0.7}_{-0.6})$, $(2.04^{+0.41}_{-0.36})$, (2.5 ± 0.7) from PTAs; $(2.0^{+0.7}_{-0.5})$, $(1.7^{+0.5}_{-0.4})$, $(1.3^{+0.4}_{-0.3})$, $(1.4^{+0.5}_{-0.4})$ from the four M_*-based GSMFs; and $(1.1^{+0.4}_{-0.3})$, $(2.5^{+1.5}_{-0.8})$ from the σ-based GSMFs.

where $\langle q/(1+q)^2 \rangle = \int dq\, p_q q/(1+q)^2$ and $\langle (1+z)^{-1/3} \rangle = \int dz\, p_z(1+z)^{-1/3}$. Sato-Polito et al. (2023) adopt $p_z(z) \propto z^\gamma e^{-z/z_*}$ with $\gamma = 0.5$ and $z_* = 0.3$ and $p_q(q) \propto q^\delta$ for $0.1 < q < 1$ with $\delta = -1$. The two distributions peak at $z \sim 0.3$ and $q = 0.1$, and $\langle q/(1+q)^2 \rangle = 0.178$ and $\langle (1+z)^{-1/3} \rangle = 0.894$. In comparison, the SMBH population synthesis modeling in Agazie et al. (2023b) finds the source contribution to h_c^2 to be peaked near $z \sim 1$ and $q \sim 1$ (see solid curves in their Figure 12). We find their distributions well approximated by

$$p_z(z) \propto z^\gamma e^{-(z/z_*)^\beta}, \quad p_q(q) \propto q^2, \tag{6}$$

and $\gamma = 1.0$, $z_* = 0.5$, and $\beta = 2$. Using these distributions yields $\langle q/(1+q)^2 \rangle = 0.238$ and $\langle (1+z)^{-1/3} \rangle = 0.890$ and raises the inferred h_c by about 14% compared to those of Sato-Polito et al. (2023). We adopt Equation (6) for the following calculations.

The amplitude h_c (at $f = 1\,\mathrm{yr}^{-1}$) computed from Equations (5) and (6) using each of the BHMFs discussed in Section 4 is displayed in the right panel of Figure 5. The first four points show that the 90% confidence intervals of h_c from the new BHMFs presented in this work (violet circle) overlap substantially with the PTA results (for a fixed spectral index of $\alpha = -2/3$). Therefore, unlike Sato-Polito et al. (2023), we do not find tension between the h_c predicted by our BHMF and reported by the PTAs. Our calculation also shows that the h_c inferred from earlier GSMFs are somewhat lower than the PTA levels, but the 90% confidence intervals largely overlap. However, when the BHMF inferred from galaxy σ distribution is used, we obtain a low h_c (filled cyan circle), consistent with the finding of Sato-Polito et al. (2023). We have also verified that their ad hoc broken power-law M_{BH}–σ relation with

$M_{\mathrm{BH}} \sim \sigma^{10.5}$ at the high-mass end indeed boosts h_c to be compatible with PTA values (open cyan circle).

The origin of the differing h_c is illustrated in the left panel of Figure 5, where we plot the differential contribution to h_c^2, $dh_c^2/d\log_{10}M_{\mathrm{BH}}$, as a function of M_{BH} for each model. For all the calculations based on GSMFs, the contributions to h_c peak at $M_{\mathrm{BH}} \sim (1–3) \times 10^9\,M_\odot$. The main difference among the various GSMFs is the height of this peak. The σ-based BHMF has a different shape and a lower amplitude at $M_{\mathrm{BH}} \lesssim 5 \times 10^9\,M_\odot$ than all the M_*-based BHMFs (top panel of Figure 4), leading to a lower peak in the mass range $M_{\mathrm{BH}} \sim (1–5) \times 10^9\,M_\odot$ that contributes the most to h_c. In comparison, the ad hoc model of Sato-Polito et al. (2023), which is designed to match PTA results, moves the peak of the h_c contribution to $M_{\mathrm{BH}} \sim 3 \times 10^{10}\,M_\odot$ (dotted cyan curve), hence their requirement of a population of $3 \times 10^{10}\,M_\odot$ SMBHs. By contrast, our GSMF and BHMF are able to match the PTA levels by having a higher amplitude of GSMF at $M_* \sim 10^{12}\,M_\odot$ and a higher amplitude of BHMF at $M_{\mathrm{BH}} \sim 2 \times 10^9\,M_\odot$ without the need for a population of unobserved ultramassive SMBHs in the local volume.

As a final note, we perform a quick estimate of h_c by approximating the BHMF as a broken power law over the masses where the majority of the contribution to h_c lies. Our BHMF is roughly $dn/d\log_{10}M_{\mathrm{BH}} \propto M_{\mathrm{BH}}^{-1.1}$ for $10^{7.5}\,M_\odot < M_{\mathrm{BH}} < 10^{9.5}\,M_\odot$ and $\propto M_{\mathrm{BH}}^{-2.5}$ for $10^{9.5}\,M_\odot < M_{\mathrm{BH}} < 10^{10.5}\,M_\odot$, where the amplitude at $M_{\mathrm{BH}} = 10^{9.5}\,M_\odot$ is $\sim 2 \times 10^{-4}\,\mathrm{Mpc}^{-3}$. Using this approximation and the simplifying assumption of $q = 1$ and $z = 1$ in Equation (5), we find $h_c \sim 1.9 \times 10^{-15}$, which is within $\sim 5\%$ of $h_c = 2.0 \times 10^{-15}$ from our more careful calculation.

5.2. Local Black Hole Mass Density

Various approaches have been taken to estimate the local mass density of SMBHs from the properties of galaxies (see
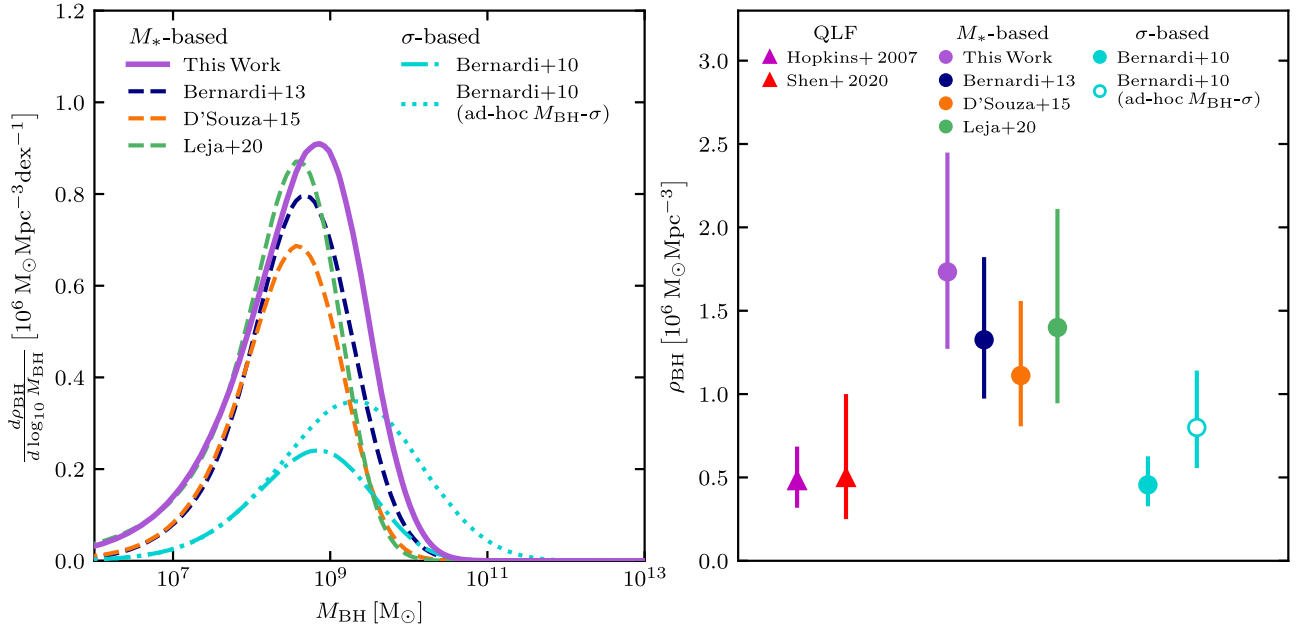
Figure 6. Comparison of the local black hole mass density, ρ_{BH}, given by each BHMF in Figure 4 and inferred from the QLF. The right panel shows ρ_{BH}, and the left panel shows the differential contribution to ρ_{BH}, $d\rho_{BH}/d\log_{10}M_{BH}$, as a function of M_{BH}. All error bars denote 90% confidence intervals. Hopkins et al. (2007) quotes a 68% interval; we enlarge it by a factor of 1.64 to approximate the 90% interval.

review by Kelly & Merloni 2012 and references therein). One common method uses the properties of quasars and links SMBH mass growth to the quasar luminosity function (QLF) via some variation on the Sołtan argument (Sołtan 1982). The estimates have typically yielded an SMBH mass density in the range of $\rho_{BH} = (2–6.5) \times 10^5 \ M_\odot \, \mathrm{Mpc}^{-3}$ if the quasar mass-to-energy conversion efficiency is assumed to be $\epsilon \sim 0.1$ (e.g., Salucci et al. 1999; Yu & Tremaine 2002; Marconi et al. 2004; Shankar et al. 2004; Hopkins et al. 2007). A recent update to Hopkins et al. (2007) using a newer quasar SED model, bolometric and extinction corrections, and binned estimations of the QLF finds a factor of ~4 uncertainty: $\rho_{BH} = (2.5–10) \times 10^5 \ M_\odot \, \mathrm{Mpc}^{-3}$ (Shen et al. 2020).

Another approach to estimate the local ρ_{BH} takes into account the entire local galaxy population (as we have done in this Letter). The SMBH mass density is obtained by convolving the distribution function of a galaxy property (e.g., velocity dispersion σ, luminosity L, stellar mass M_*) with a scaling relation between that galaxy property and M_{BH}. Yu & Tremaine (2002) find the σ-based density to be $\rho_{BH} = (2.9 \pm 0.5) \times 10^5 \ M_\odot \, \mathrm{Mpc}^{-3}$ and the L-based density to be $\rho_{BH} = 6.3 \times 10^5 \ M_\odot \, \mathrm{Mpc}^{-3}$ (after scaling their results to $h = 0.7$). While Yu & Tremaine (2002) favor galaxy σ as the M_{BH} predictor, a subsequent study by Lauer et al. (2007) advocates galaxy L as the M_{BH} predictor and finds $\rho_{BH} = 4.4 \times 10^5 \ M_\odot \, \mathrm{Mpc}^{-3}$ with similar calculations but updated data. They report a lower value of $\rho_{BH} = 1.6 \times 10^5 \ M_\odot \, \mathrm{Mpc}^{-3}$ when σ is used. A compilation of results from various galaxy indicators and data obtains $\rho_{BH} = (3.2–5.4) \times 10^5 \ M_\odot \, \mathrm{Mpc}^{-3}$ (Shankar et al. 2009).

The right panel of Figure 6 shows our estimates of ρ_{BH} from integration of the BHMFs presented in Figure 4; the left panel shows the corresponding differential contribution $d\rho_{BH}/d\log_{10}M_{BH}$ as a function of M_{BH}. The M_*-based values for ρ_{BH} are all above $\sim 10^6 \ M_\odot \, \mathrm{Mpc}^{-3}$, with $\rho_{BH} = (1.8^{+0.8}_{-0.5}) \times 10^6 M_\odot \, \mathrm{Mpc}^{-3}$ for our BHMF, and the differential contributions to ρ_{BH} all peak at $M_{BH} \sim 10^{8.5}$–

$10^9 \ M_\odot$. Our σ-based $\rho_{BH} = (4.55^{+1.71}_{-1.28}) \times 10^5 M_\odot \, \mathrm{Mpc}^{-3}$ is lower by a factor of 2 or more (filled cyan circle), similar to the difference between the σ and L predictors discussed above. Our σ-based value is about 50% higher than the σ-based value of Yu & Tremaine (2002) largely because of the steeper slope of the M_{BH}–σ relation in McConnell & Ma (2013) than in Tremaine et al. (2002). A similarly steep M_{BH}–σ relation is reported in Saglia et al. (2016), which we find to give essentially the same ρ_{BH} as ours.

A notable trend in Figure 6 is that all ρ_{BH} inferred from BHMFs based on galaxy stellar masses are significantly higher than the values based on QLF discussed above (two examples shown as triangles). Since the mass acquired during the bright quasar phases scales roughly inversely with the assumed radiative efficiency ϵ, one way to match the high values of the local ρ_{BH} found in this Letter is to have $\epsilon \lesssim 0.03$. Shankar et al. (2013) examine but reject a model in which ϵ decreases from ~ 0.14 at high redshift to ~ 0.004 at the present day because it suggests a larger relic BHMF than their data at most mass scales. Alternatively, raising the obscuration fraction of AGNs can help boost the inferred local ρ_{BH}.

6. Conclusions

We have presented a new $z = 0$ GSMF and calculated the inferred local BHMF, number of massive SMBHs, SMBH mass density, and amplitude of the stochastic gravitational-wave background probed by PTA teams. Our GSMF is constructed to match the observed distribution of stellar masses of MASSIVE galaxies at $M_* \gtrsim 10^{11.5} \ M_\odot$. We have incorporated two sets of M_* measurements from dynamical modeling and SPS modeling and used them to calibrate the M_*–M_K relation for the whole MASSIVE sample. These state-of-the-art M_* measurements are obtained from high-S/N and spatially resolved stellar spectroscopic data and detailed modeling.

Encouragingly, we find that the average M_* from these two independent methods differs by only $\sim$7% (Figure 1).

While prior $z \sim 0$ GSMFs differ significantly from one another at $M_* \gtrsim 10^{11.3}\ M_\odot$, our GSMF has the highest number density of massive galaxies (Figure 3). These prior studies measure M_* from photometric data using a variety of SED and SPS fitting methods assuming a Chabrier-like or Kroupa-like IMF. The spectroscopic study of Gu et al. (2022), however, finds the IMF of MASSIVE galaxies to be steeper than the Milky Way IMF with an average mismatch parameter of $\alpha_{\rm IMF} \equiv (M/L)/(M/L)_{\rm MW} = 1.84$. While a reanalysis of prior work with a bottom-heavy IMF is needed to better understand the origin of the differing GSMFs, we note that a simple shift in M_* rightward by a factor of $\alpha_{\rm IMF}$ in the high-mass portion of the Bernardi et al. (2013) and D'Souza et al. (2015) curves in Figure 3 would bring them close to our GSMF. A factor of 2.5–3 increase in M_*, however, would be needed for the high-mass end of the $z = 0$ Leja et al. (2020) GSMF to match ours. Thus, even if we assume the same $\alpha_{\rm IMF}$ correction factor at $z \sim 1$ and shift their $z \sim 1$ GSMF accordingly, there would still be notable mass growths in massive galaxies between their $z \sim 1$ GSMF and our $z \sim 0$ GSMF. Our GSMF therefore largely resolves the inconsistency between a lack of evolution in prior GSMFs between $z \sim 1$ and $z = 0$ and the mass growth over these 8 billion yr expected from galaxy formation models and simulations.

The BHMF derived from our GSMF (Figure 4) predicts $\sim$1–10 SMBHs with $M_{\rm BH} \gtrsim 10^{10}\ M_\odot$ in the MASSIVE survey volume, fully consistent with the current known SMBH population at the highest masses. The characteristic amplitude of nanohertz gravitational waves due to SMBH binary mergers inferred from our BHMF is also consistent with the levels reported by the PTAs (Figure 5). However, we find a substantially smaller h_c when galaxy velocity dispersion is used as a proxy for $M_{\rm BH}$. It has been noted that galaxy velocity dispersions tend to underpredict $M_{\rm BH}$ in massive galaxies compared with galaxy luminosities or stellar masses (e.g., Lauer et al. 2007). A plausible explanation is that gas-poor mergers of elliptical galaxies that are primarily responsible for the formation of local massive galaxies can easily increase L and M_* while changing σ slowly (e.g., Boylan-Kolchin et al. 2006). Galaxy σ is therefore likely to be a less robust indicator of $M_{\rm BH}$ for very massive galaxies in the local Universe.

While our new $z = 0$ GSMF leads to a concordant picture in the high-mass end of the local galaxy and SMBH populations and the gravitational-wave background from merging SMBHs, one intriguing difference is that the local SMBH mass densities inferred from our and other GSMFs are notably higher than the SMBH mass density estimated from quasars (Figure 6). We leave this topic to future investigations.

Appendix A
Dynamical Masses of MASSIVE Galaxies

Table A1 lists galaxies in the MASSIVE survey with masses that have been determined from dynamical modeling.

Table A1
Dynamical Masses of MASSIVE Galaxies

Name (1)	$D_{\rm M14}$ (Mpc) (2)	$D_{\rm SBF}$ (Mpc) (3)	$D_{\rm literature}$ (Mpc) (4)	$M_K^{\rm 2MASS}$ (mag) (5)	$M_K^{\rm CFHT}$ (mag) (6)	$M_{\rm BH}$ ($10^9\ M_\odot$) (7)	$M_*^{\rm dyn}$ ($10^{11}\ M_\odot$) (8)	Method (9)	Reference (10)
NGC 57	76.3	66.9	66.8	−25.75	−25.75		3.73*	Tri. stellar orbit	J. Pilawa et al. 2024, in preparation
NGC 315	70.3	68.1	70.0	−26.30	−26.48	2.02	11.70*	CO gas	Boizelle et al. (2021)
NGC 708	69.0	61.5	68.5	−25.65	−25.55	8.98	2.51*	Tri. stellar orbit	de Nicola et al. (2024)
NGC 997	90.4	83.7*	90.4	−25.40	−25.68	3.28		CO gas	Dominiak et al. (2024)
NGC 1453	56.4	51.2	51.0	−25.67	−25.64	2.91	3.28*	Tri. stellar orbit	Quenneville et al. (2022)
	56.4	51.2	51.0	−25.67	−25.64	2.91	3.39	Axi. stellar orbit	Liepold et al. (2020)
	56.4	51.2	56.4	−25.67	−25.64	2.99	3.65	Axi. stellar Jeans	Ene et al. (2019)
NGC 1600	63.8	71.7	64.0	−25.99	−26.62	19.05	9.30*	Axi. stellar orbit	Thomas et al. (2016)
NGC 1684	63.5	62.8	62.8	−25.34	−25.70	1.40		CO gas	Dominiak et al. (2024)
NGC 2693	74.4	71.0	71.0	−25.76	−25.72	1.70	7.19*	Tri. stellar orbit	Pilawa et al. (2022)
	74.4	71.0	71.0	−25.76	−25.72	2.40	6.94	Axi. stellar orbit	Pilawa et al. (2022)
	74.4	71.0	71.0	−25.76	−25.72	2.90	6.64	Axi. stellar Jeans	Pilawa et al. (2022)
NGC 3842	99.4	87.5	98.4	−25.91	−25.93	8.63	13.78*	Axi. stellar orbit	McConnell et al. (2011)
NGC 4472	16.7	16.7	17.1	−25.72	−25.83	2.44	5.58*	Axi. stellar orbit	Rusli et al. (2013)
	16.7	16.7	17.1	−25.72	−25.83		5.82†	Axi. stellar Jeans	Cappellari et al. (2013)
M87	16.7	16.7	16.8	−25.31	−25.44	5.34	3.95*	Tri. stellar orbit	Liepold et al. (2023)
	16.7	16.7	17.9	−25.31	−25.44	6.16	9.86	Axi. stellar orbit	Gebhardt et al. (2011)
	16.7	16.7	17.9	−25.31	−25.44	3.27		Ionized gas	Walsh et al. (2013)
	16.7	16.7	17.2	−25.31	−25.44		5.18†	Axi. stellar Jeans	Cappellari et al. (2013)
NGC 4649	16.5	16.5	15.7	−25.36	−25.48	4.73	7.96*	Axi. stellar orbit	Shen & Gebhardt (2010)
	16.5	16.5	17.3	−25.36	−25.48		4.99†	Axi. stellar Jeans	Cappellari et al. (2013)
NGC 4889	102.0	99.1	103.2	−26.64	−26.74	20.17	16.80*	Axi. stellar orbit	McConnell et al. (2011)
NGC 5322	34.2	31.5	30.3	−25.51	−25.43		3.54†	Axi. stellar Jeans	Cappellari et al. (2013)
NGC 5353	41.1	34.8	35.2	−25.45	−25.31		3.15†	Axi. stellar Jeans	Cappellari et al. (2013)
NGC 5557	51.0	49.2	38.8	−25.46	−25.68		2.73†	Axi. stellar Jeans	Cappellari et al. (2013)

Table A1
(Continued)

Name	D_{M14} (Mpc)	D_{SBF} (Mpc)	$D_{literature}$ (Mpc)	M_K^{2MASS} (mag)	M_K^{CFHT} (mag)	M_{BH} ($10^9\ M_\odot$)	M_*^{dyn} ($10^{11}\ M_\odot$)	Method	Reference
(1)	(2)	(3)	(4)	(5)	(6)	(7)	(8)	(9)	(10)
NGC 7052	69.3	61.9	58.7	−25.67	−25.63		$3.06^\dagger$	Sph. stellar Jeans	Häring & Rix (2004)
	69.3	61.9	58.7	−25.67	−25.63	0.35		Ionized gas	vdM+vdB (1998)
NGC 7619	54.0	46.6	51.5	−25.65	−25.68	2.26	4.98^*	Axi. stellar orbit	Rusli et al. (2013)

Note. Column (1): MASSIVE galaxy name. Column (2): distance from MASSIVE survey paper Ma et al. (2014), which adopts SBF distance if available and group-corrected flow velocities otherwise. Column (3): updated distance from Quenneville et al. (2024), all by the SBF method except NGC 997, for which the non-SBF distance is corrected as described in Section 2.4. Column (4): distance assumed in the dynamical modeling literature. Column (5): extinction-corrected total absolute K-band magnitude derived from 2MASS XSC apparent K-band magnitude (parameter k_m_ext; column (5) of Table 3 in Ma et al. 2014) and distance in column (3). Column (6): absolute K-band magnitude derived from CFHT apparent K-band magnitude (column (6) of Table A1 in Quenneville et al. 2024) and distance in column (3). Column (7): black hole mass from dynamical modeling, corrected to distance in column (3). Column (8): total stellar mass from dynamical modeling, corrected to distance in column (3). Symbol $\dagger$ indicates total dynamical mass when the mass of the stellar component is unavailable. The 11 mass measurements used in Section 2 are indicated with asterisks. Column (9): method used for dynamical modeling. "Tri." for triaxial, "Axi." for axisymmetric, "Sph." for spherical. Column (10): dynamical modeling reference.

Appendix B
The Stellar Mass Function

The GSMF in this work has a double Schechter form (Equation (2)). To determine the parameters in this function, we use the procedure of Section 4.2 of Leja et al. (2020) and model the MASSIVE observations as the result of an inhomogeneous Poisson process whose rate function is a product of the GSMF and the differential comoving volume. As discussed in Section 2.4, when using masses inferred from M_K^{CFHT}, we use distances that have been homogenized with the SBF measurements to compute the differential comoving volumes. We add a χ^2-like term to the log-likelihood that is associated with the mismatch between the proposed GSMF and that of Leja et al. (2020) at three stellar masses: 10^9, 10^{10}, and $10^{11}\ M_\odot$. This choice of points approximately recovers the 90% error band of their GSMF between $10^9\ M_\odot$ and $10^{11}\ M_\odot$ without significantly degrading the fit to the MASSIVE data at high masses.

We use dynesty (Speagle 2020) to sample the posterior distribution for the five model parameters ϕ_1, ϕ_2, α_1, α_2, and M_s. The posterior distribution exhibits a strong correlation between the amplitude and power-law slope of the high-mass component, ϕ_1 and α_1. This correlation is due to the fact that the high-stellar-mass observations in MASSIVE lie well above the preferred scale radius M_s, where the shape of the GSMF is largely set by the exponential term and changes in the power-law slope result primarily in a change in the amplitude of the component rather than a change to the shape of the function. Accordingly, the power-law slope and the amplitude of the high-mass component are correlated in our posterior distribution.

Because of this, approximating the posterior on these parameters as uncorrelated will significantly overrepresent the true uncertainty in the GSMF. However, when ϕ_1 and ϕ_2 are replaced with the amplitudes of the GSMF at two widely separated mass scales, e.g., $M_L = 10^{10}\ M_\odot$ and $M_H = 10^{12}\ M_\odot$, we find the posterior to be reasonably well approximated with uncorrelated Gaussians. We perform the posterior sampling using the standard parameters (ϕ_1, ϕ_2, M_s, α_1, α_2) and present the inferred values on these parameters and the values of the GSMF at $10^{10}\ M_\odot$ and $10^{12}\ M_\odot$ (ϕ_L and ϕ_H) in Table B1.

When reproducing the posterior distribution of our GSMF fit parameters, we recommend drawing uncorrelated Gaussian distributions for (ϕ_L, ϕ_H, M_s, α_1, α_2) with the centers and widths listed in Table B1 and then using the following script to map these parameters into the standard ϕ_1 and ϕ_2 that appear in Equation (2). For comparison, when the full posterior

Table B1
Posteriors for Double Schechter Parameters for GSMFs

	GSMF in Leja et al. (2020)		GSMF in This Letter		
	$z = 0.2$	$z = 0.0$	Dyn. M_*	SPS M_*	Combined M_*
$\log_{10}(\phi_1/\mathrm{Mpc}^{-3})$	−2.44 ± 0.02	−2.38 ± 0.03	−4.83 ± 0.50	−4.87 ± 0.60	−4.85 ± 0.55
$\log_{10}(\phi_2/\mathrm{Mpc}^{-3})$	$-2.89^{+0.03}_{-0.04}$	−2.82 ± 0.05	−2.87 ± 0.09	−2.84 ± 0.08	−2.85 ± 0.09
$\log_{10}(M_s/M_\odot)$	10.79 ± 0.02	10.77 ± 0.03	11.34 ± 0.06	11.31 ± 0.06	11.33 ± 0.06
α_1	−0.28 ± 0.07	−0.28 ± 0.07	1.08 ± 0.77	0.84 ± 0.96	0.92 ± 0.90
α_2	$-1.48^{+0.01}_{-0.02}$	$-1.48^{+0.01}_{-0.02}$	−1.38 ± 0.04	−1.37 ± 0.04	−1.38 ± 0.04
$\log_{10}(\phi_L/\mathrm{Mpc}^{-3})$	−2.10 ± 0.04	−2.04 ± 0.04	−2.01 ± 0.03	−2.01 ± 0.03	−2.01 ± 0.03
$\log_{10}(\phi_H/\mathrm{Mpc}^{-3})$	−8.25 ± 0.32	−8.57 ± 0.43	−4.45 ± 0.09	−4.59 ± 0.11	−4.52 ± 0.12

Note. Posterior distributions for the parameters of the double Schechter approximation to five GSMFs. The bottom two rows list GSMF amplitudes at two reference masses, ϕ_L at $M_L = 10^{10}\ M_\odot$ and ϕ_H at $M_H = 10^{12}\ M_\odot$. Column (1): parameter names. Column (2): $z = 0.2$ GSMF of Leja et al. (2020). Column (3): our extrapolation of Leja et al. (2020) to $z = 0$. Column (4): GSMF of this Letter constructed from the lower-mass part of the $z = 0$ GSMF of Leja et al. (2020) and the MASSIVE GSMF at higher masses using dynamically inferred M_* for MASSIVE galaxies. Column (5): same as column (4) but for MASSIVE SPS inferred M_*. Column (6): the fiducial GSMF of this Letter, combining the two posteriors of columns (4) and (5). All errors denote 68% confidence intervals.

distribution is used, the 90% error band of the GSMF for dynamical M_* is on average 0.39 dex wide between $10^{11.5}\,M_\odot$ and $10^{12.5}\,M_\odot$, while it is 0.47 dex wide when using the scheme described below and is inflated to 1.16 dex wide when naively drawing α_1 and ϕ_1 as uncorrelated variables.

Finally, we combine the posteriors when inferring stellar masses from SPS-based measurements and dynamical measurements. This is trivially done by drawing half of the realizations of the combined posterior from the SPS-based posterior and half from the dynamical-M_*-based posterior.

For ease of reproduction, we have provided below a short section of `python` code that can be used to approximate the posteriors of the parameters of our GSMF.

```python
import numpy as np

def compute_phi1_phi2(
    phi_L,
    phi_H,
    alph_1,
    alph_2,
    log_Ms,
    log_ML=10,
    log_MH=12):

    tL=10**(log_ML-log_Ms)
    tH=10**(log_MH-log_Ms)

    l_1L=np.exp(-tL)*tL**(alph_1+1)
    l_1H=np.exp(-tH)*tH**(alph_1+1)
    l_2L=np.exp(-tL)*tL**(alph_2+1)
    l_2H=np.exp(-tH)*tH**(alph_2+1)

    denominator=np.log(10) * \
      (l_1L*l_2H-l_1H*l_2L)

    phi1=l_2H*phi_L-l_2L*phi_H /\
      denominator
    phi2=l_1L*phi_H-l_1H*phi_L /\
      denominator

    phi1[phi1 < 0]=1e-10
    phi2[phi2 < 0]=1e-10

    return(phi1, phi2)

n_post_realizations=1000000
n_post_dyn_realizations=n_post_realizations // 2
n_post_sps_realizations=n_post_realizations // 2

# These values are from Table B1

post_dyn_values=np.array([
  [-2.01, 0.03],
  [-4.52, 0.12],
  [ 0.92, 0.90],
  [-1.38, 0.04],
  [11.33, 0.06],
  ])

post_sps_values=np.array([
  [-2.01, 0.03],
  [-4.59, 0.11],
  [ 0.84, 0.96],
  [-1.37, 0.04],
  [11.31, 0.06],
  ])

post_dyn_realizations=np.random.normal(
```

(Continued)

```python
    post_dyn_values[:, 0],
    post_dyn_values[:, 1],
    size=(n_post_dyn_realizations, 5))

post_sps_realizations=np.random.normal(
    post_sps_values[:, 0],
    post_sps_values[:, 1],
    size=(n_post_sps_realizations, 5))

posterior_realizations=np.r_[
    post_dyn_realizations,post_sps_realizations
    ]

posterior_realizations[:, :2]=\
    10**posterior_realizations[:, :2]

posterior_realizations[:, 0], \
  posterior_realizations[:, 1]=\
    compute_phi1_phi2(*posterior_realizations.T)

posterior_realizations[:, :2]=\
    np.log10(posterior_realizations[:, :2])
```

ORCID iDs

Emily R. Liepold ⓘ https://orcid.org/0000-0002-7703-7077
Chung-Pei Ma ⓘ https://orcid.org/0000-0002-4430-102X

References

Agazie, G., Anumarlapudi, A., Archibald, A. M., et al. 2023a, ApJL, 951, L8
Agazie, G., Anumarlapudi, A., Archibald, A. M., et al. 2023b, ApJL, 952, L37
Baldry, I. K., Driver, S. P., Loveday, J., et al. 2012, MNRAS, 421, 621
Bernardi, M., Meert, A., Sheth, R. K., et al. 2013, MNRAS, 436, 697
Bernardi, M., Shankar, F., Hyde, J. B., et al. 2010, MNRAS, 404, 2087
Blakeslee, J. P., Jensen, J. B., Ma, C.-P., Milne, P. A., & Greene, J. E. 2021, ApJ, 911, 65
Blanton, M. R., Schlegel, D. J., Strauss, M. A., et al. 2005, AJ, 129, 2562
Boizelle, B. D., Walsh, J. L., Barth, A. J., et al. 2021, ApJ, 908, 19
Boylan-Kolchin, M., Ma, C.-P., & Quataert, E. 2006, MNRAS, 369, 1081
Bundy, K., Leauthaud, A., Saito, S., et al. 2017, ApJ, 851, 34
Cappellari, M. 2013, ApJL, 778, L2
Cappellari, M., et al. 2011, MNRAS, 413, 813
Cappellari, M., Scott, N., Alatalo, K., et al. 2013, MNRAS, 432, 1709
Crook, A. C., Huchra, J. P., Martimbeau, N., et al. 2007, ApJ, 655, 790
Davidzon, I., Ilbert, O., Laigle, C., et al. 2017, A&A, 605, A70
de Nicola, S., Thomas, J., Saglia, R. P., et al. 2024, MNRAS, 530, 1035
Dominiak, P., Bureau, M., Davis, T. A., et al. 2024, MNRAS, 529, 1597
D'Souza, R., Vegetti, S., & Kauffmann, G. 2015, MNRAS, 454, 4027
Ene, I., Ma, C.-P., McConnell, N. J., et al. 2019, ApJ, 878, 57
Ene, I., Ma, C.-P., Walsh, J. L., et al. 2020, ApJ, 891, 65
Ene, I., Ma, C.-P., Veale, M., et al. 2018, MNRAS, 479, 2810
EPTA CollaborationInPTA Collaboration, Antoniadis, J., et al. 2023, A&A, 678, A50
Fitzpatrick, E. L. 1999, PASP, 111, 63
Gebhardt, K., Adams, J., Richstone, D., et al. 2011, ApJ, 729, 119
Goullaud, C. F., Jensen, J. B., Blakeslee, J. P., et al. 2018, ApJ, 856, 11
Gu, M., Greene, J. E., Newman, A. B., et al. 2022, ApJ, 932, 103
Häring, N., & Rix, H.-W. 2004, ApJL, 604, L89
Hopkins, P. F., Richards, G. T., & Hernquist, L. 2007, ApJ, 654, 731
Huchra, J. P., Macri, L. M., Masters, K. L., et al. 2012, ApJS, 199, 26
Jarrett, T. H., Chester, T., Cutri, R., et al. 2000, AJ, 119, 2498
Jensen, J. B., Blakeslee, J. P., Ma, C.-P., et al. 2021, ApJS, 255, 21
Kelly, B. C., & Merloni, A. 2012, AdAst, 2012, 970858
Laigle, C., McCracken, H. J., Ilbert, O., et al. 2016, ApJS, 224, 24
Lauer, T. R., Faber, S. M., Richstone, D., et al. 2007, ApJ, 662, 808
Leja, J., Speagle, J. S., Johnson, B. D., et al. 2020, ApJ, 893, 111
Li, C., & White, S. D. M. 2009, MNRAS, 398, 2177
Liepold, E. R., Ma, C.-P., & Walsh, J. L. 2023, ApJL, 945, L35

Liepold, E. R., Quenneville, M. E., Ma, C.-P., et al. 2020, ApJ, 891, 4
Ma, C.-P., Greene, J. E., McConnell, N., et al. 2014, ApJ, 795, 158
Marconi, A., Risaliti, G., Gilli, R., et al. 2004, MNRAS, 351, 169
McConnell, N. J., Chen, S.-F. S., Ma, C.-P., et al. 2013, ApJL, 768, L21
McConnell, N. J., & Ma, C.-P. 2013, ApJ, 764, 184
McConnell, N. J., Ma, C.-P., Gebhardt, K., et al. 2011, Natur, 480, 215
Mehrgan, K., Thomas, J., Saglia, R., et al. 2024, ApJ, 961, 127
Mortlock, A., Conselice, C. J., Hartley, W. G., et al. 2015, MNRAS, 447, 2
Moustakas, J., Coil, A. L., Aird, J., et al. 2013, ApJ, 767, 50
Moustakas, J., Lang, D., Schlegel, D. J., et al. 2021, AAS Meeting Abstracts, 53, 527.04
Moustakas, J., Lang, D., Dey, A., et al. 2023, ApJS, 269, 3
Muzzin, A., Marchesini, D., Stefanon, M., et al. 2013, ApJ, 777, 18
Phinney, E. S. 2001, arXiv:astro-ph/0108028
Pilawa, J. D., Liepold, E. R., Delgado Andrade, S. C., et al. 2022, ApJ, 928, 178
Pozzetti, L., Bolzonella, M., Zucca, E., et al. 2010, A&A, 523, A13
Quenneville, M. E., Blakeslee, J. P., Ma, C.-P., et al. 2024, MNRAS, 527, 249
Quenneville, M. E., Liepold, E. R., & Ma, C.-P. 2022, ApJ, 926, 30
Reardon, D. J., Zic, A., Shannon, R. M., et al. 2023, ApJ, 951, L6
Rusli, S. P., Thomas, J., Saglia, R. P., et al. 2013, AJ, 146, 45
Saglia, R. P., Opitsch, M., Erwin, P., et al. 2016, ApJ, 818, 47
Salucci, P., Szuszkiewicz, E., Monaco, P., & Danese, L. 1999, MNRAS, 307, 637
Santini, P., Fontana, A., Grazian, A., et al. 2012, A&A, 538, A33
Sato-Polito, G., Zaldarriaga, M., & Quataert, E. 2023, arXiv:2312.06756
Schlafly, E. F., & Finkbeiner, D. P. 2011, ApJ, 737, 103
Shankar, F., Salucci, P., Granato, G. L., De Zotti, G., & Danese, L. 2004, MNRAS, 354, 1020
Shankar, F., Weinberg, D. H., & Miralda-Escudé, J. 2009, ApJ, 690, 20
Shankar, F., Weinberg, D. H., & Miralda-Escudé, J. 2013, MNRAS, 428, 421
Shen, J., & Gebhardt, K. 2010, ApJ, 711, 484
Shen, X., Hopkins, P. F., Faucher-Giguère, C.-A., et al. 2020, MNRAS, 495, 3252
Skelton, R. E., Whitaker, K. E., Momcheva, I. G., et al. 2014, ApJS, 214, 24
Skrutskie, M. F., Cutri, R. M., Stiening, R., et al. 2006, AJ, 131, 1163
Soltan, A. 1982, MNRAS, 200, 115
Speagle, J. S. 2020, MNRAS, 493, 3132
Thomas, J., Ma, C.-P., McConnell, N. J., et al. 2016, Nature, 532, 340
Tomczak, A. R., Quadri, R. F., Tran, K.-V. H., et al. 2014, ApJ, 783, 85
Tremaine, S., et al. 2002, ApJ, 574, 740
van der Marel, R. P., & van den Bosch, F. C. 1998, AJ, 116, 2220
Vazdekis, A., Ricciardelli, E., Cenarro, A. J., et al. 2012, MNRAS, 424, 157
Veale, M., Ma, C.-P., Greene, J. E., et al. 2017a, MNRAS, 471, 1428
Veale, M., Ma, C.-P., Greene, J. E., et al. 2018, MNRAS, 473, 5446
Veale, M., Ma, C.-P., Thomas, J., et al. 2017b, MNRAS, 464, 356
Walsh, J. L., Barth, A. J., Ho, L. C., & Sarzi, M. 2013, ApJ, 770, 86
Walsh, J. L., van den Bosch, R. C. E., Gebhardt, K., et al. 2015, ApJ, 808, 183
Walsh, J. L., van den Bosch, R. C. E., Gebhardt, K., et al. 2017, ApJ, 835, 208
Walsh, J. L., van den Bosch, R. C. E., Gebhardt, K., et al. 2016, ApJ, 817, 2
Wright, A. H., Driver, S. P., & Robotham, A. S. G. 2018, MNRAS, 480, 3491
Yu, Q., & Tremaine, S. 2002, MNRAS, 335, 965